

# Critical points, phase transitions and water-like anomalies for an isotropic two length scale potential with increasing attractive well

L. Pinheiro,<sup>1</sup> A. P. Furlan,<sup>1</sup> L. B. Krott,<sup>2</sup> A. Diehl,<sup>3</sup> and M. C. Barbosa<sup>1</sup>

<sup>1</sup>*Instituto de Física, Univeridade Federal do Rio Grande do Sul,  
Caixa Postal 15051, CEP 91501-570, Porto Alegre, RS, Brazil.*

<sup>2</sup>*Centro Araranguá, Universidade Federal de Santa Catarina,  
Rua Pedro João Pereira, 150, CEP 88905-120, Araranguá, SC, Brazil*

<sup>3</sup>*Departamento de Física, Instituto de Física e Matemática,  
Universidade Federal de Pelotas, Caixa Postal 354, CEP 96010-900 Pelotas, RS, Brazil*

## Abstract

Molecular Dynamic and Monte Carlo studies are performed in a family of core-softened (CS) potential, composed by two length scales: a repulsive shoulder at short distances and the another a variable scale, that can be repulsive or strongly attractive depending on the parameters used. The density, diffusion and structural anomalous regions in the pressure versus temperature phase diagram shrink in pressure as the system becomes more attractive. The liquid-liquid transition appears as a consequence of the non monotonic behavior of the density versus pressure isotherms with the increase of the attraction well. We found that the liquid-gas phase transition is Ising-like for all the CS potentials and its critical temperature increases with the increase of the attraction. No Ising-like behavior for the liquid-liquid phase transition was detected in the Monte Carlo simulations what might be due to the presence of stable solid phases.

*Keywords:* water anomalies, phase transitions, core-softened potentials

## I. INTRODUCTION

The description of a single component system as particles interacting via a core-softened (CS) two-body potentials has been used as a viable strategy to understand the mechanism behind universal phenomena in anomalous liquids. These potentials exhibit a repulsive core with a softening region with a shoulder or a ramp [1]. These models originate from the desire to construct a simple two-body isotropic potential capable of the density [2–4] and diffusion [4–6] anomalies present in water. Another motivation for these studies is the acknowledged possibility that some single component systems display coexistence between two different liquid phases [7–12]. The use of two length scale potentials seems to be an interesting tool for finding the connection between the presence of thermodynamic and dynamic anomalies and the possibility of the presence of two liquid phases.

Complementary to the thermodynamic and dynamic anomalies, water also shows an unusual behavior in its structure. While for normal liquids the system becomes more structured with the increase of the density, water shows a maximum. Such behavior can be characterized by translational order parameter  $t$  [13–15] that exhibits a region in which  $t$  decreases under compression. The entropy also shows a very peculiar behavior. The excess entropy  $S_{ex}$ , defined as the difference between the entropy  $S$  of the liquid and the ideal gas, at same density and temperature [16–25], becomes a great tool in the investigation of liquid-state anomalies [26]. The region where  $(\partial S_{ex}/\partial \rho > 0)$  on isothermal compression corresponds to an anomaly in excess entropy, indicating an existence of distinct forms of local ordering, for a high density limit, where particles are found closer to each other, and a low density region, with large average distance between particles.

The use of core-softened potentials to reveal the origin of these anomalies becomes even more interesting because the anomalies mentioned above are not exclusive of water. Studies have shown that Te [27], Ga, Bi [28], S [29, 30],  $\text{Ge}_{15}\text{Te}_{85}$  [31],  $\text{BeF}_2$  [16, 32–34], silica [13, 16, 32, 35] and silicon [36] present water-like anomalies.

The CS potentials show a variety of shapes. They can be ramp-like [37–43] or continuous shoulder-like [19–21, 44–52]. Even though these works show the presence of the anomalies and in some cases the existence of the second critical point but in others the two liquid phases are not present [20, 21, 48, 49, 53], the limit in which the presence of the anomalies is related to the existence of a second critical point is not clear. In this paper we employ a

family of CS potentials spanning from purely repulsive to a very attractive case and analyze the behavior of the anomalies, liquid-liquid and liquid-gas critical point indicating the

This paper is organized as follow: in Sec. **II** we introduce the model; in Sec. **III** the methods and the simulation details are described; in Sec. **IV** the results are presented; and finally, in Sec. **V**, the conclusions are given.

## II. THE MODEL

The fluid is modeled by spherical particles with diameter  $\sigma$  and mass  $m$ , that interact through a three dimensional two length scales potential given by

$$\frac{U(r_{ij})}{\epsilon} = \epsilon' \left[ \left( \frac{\sigma}{r_{ij}} \right)^{12} - \left( \frac{\sigma}{r_{ij}} \right)^6 \right] + \sum_{i=1}^k \frac{B_i}{B_i^2 + (r_{ij} - C_i)^2}, \quad (1)$$

where  $r_{ij} = |\mathbf{r}_i - \mathbf{r}_j|$  is the distance between two particles  $i$  and  $j$ . The potential is composed by a standard 12-6 Lennard-Jones (LJ) potential [54] followed by a sum of  $k$  Lorentzian distributions centered in  $C_i$  and with amplitude  $1/B_i$ . This composition of the two functions provides a repulsive shoulder at short distances and an attractive global minimum at long distances, depending on the set of parameters used.

The set of parameters were chosen in order to provide different interaction scales. The idea is to have a purely repulsive case in which no liquid-liquid or liquid-gas transitions would be present. In addition, different energy attractive wells were chosen so the liquid-gas and liquid-liquid transitions would appear. The potentials resulting from the choice of the parameters are shown in figure 1 The set of parameters that were chosen for each case is shown in table I.

Our potential as illustrated in the figure 2 was constructed to follow the two length scales Jagla's ramp potential [55] but with an smooth shape. In our parameterization the attractive part of the potential was increased so we can test the effect not only of the continuous forces but also of the depth of the attraction.

## III. SIMULATION DETAILS

Two different simulations techniques were employed: Molecular Dynamics (MD) and Grand-Canonical Monte Carlo (GCMC) simulations.

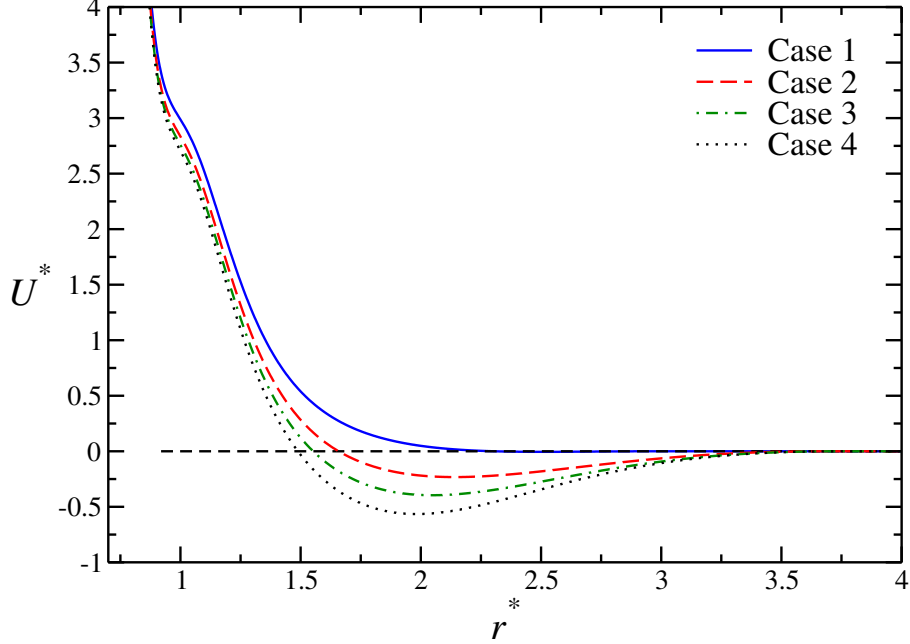


FIG. 1. All the potentials studied here. For the Case 1 there is just a repulsive shoulder at  $r^* \sim 1.0$ . For the cases 2, 3 and 4 the repulsive shoulder is also maintained at  $r^* \sim 1$ , but the attractive part is at  $r^* = 2.18, 2.10$  and  $2.06$ , respectively. The black dashed line just represent the level zero of potential.

Parameters values	Parameters values	Cases
$\epsilon' = 0.60$	$k = 3$	
$B_1 = 0.30$	$C_1 = 1.00$	
$B_2 = \begin{cases} -1.0 \\ -1.2 \\ -1.5 \\ -3.0 \end{cases}$	$C_2 = 1.80$	$\begin{cases} \text{Case 4} \\ \text{Case 3} \\ \text{Case 2} \\ \text{Case 1} \end{cases}$
$B_3 = 2.00$	$C_3 = 3.00$	

TABLE I. Parameters of the potentials studied.

### A. Molecular Dynamics in the $NVT$ Ensemble

The systems were studied using MD simulations with 512 particles in a cubic box, with the standard periodic boundary conditions in all directions. The simulations were performed

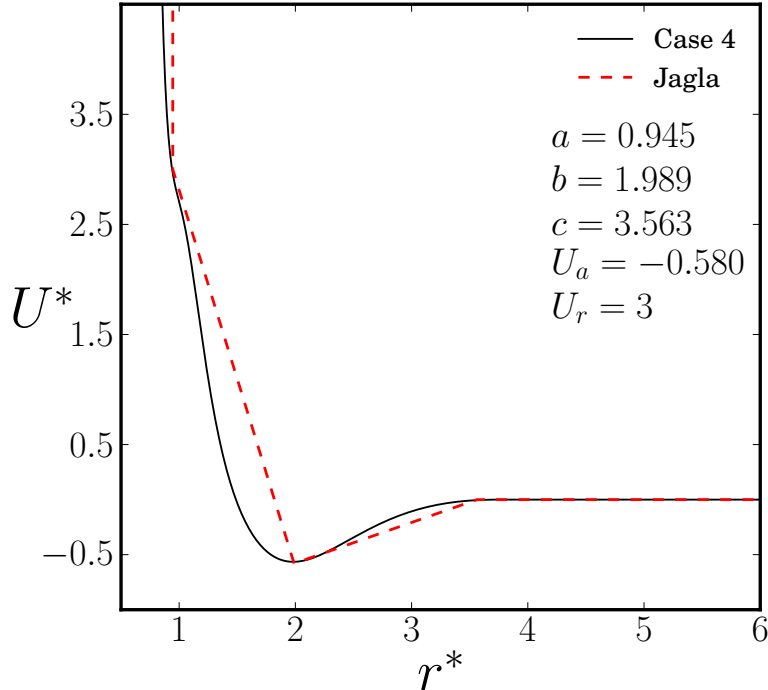


FIG. 2. Equivalence between the potential defined by Xu *et al.* [56] and our continuous potential. The interpretation of parameters can be seen by Xu *et al.* [56].

in the  $NVT$  ensemble, with the Nose-Hoover [57, 58] thermostat with coupling parameter  $Q = 2$  to keep the temperature fixed. The particle-particle interaction was considered until a characteristic cutoff radius  $r_c = 3.7$ , and the potential was shifted in order to provide  $U = 0$  at  $r_c$ . The initial configurations of the systems were chosen as liquid structures. The equilibrium state was reached after  $5 \times 10^5$  steps, followed by  $8 \times 10^5$  simulation steps for a production. For the integration of the motion equations we have used the Velocity-Verlet method [54], with time step  $\Delta t = 0.001$  in LJ reduced units. The average of the physical quantities were obtained using 50 uncorrelated samples. The thermodynamic stability of the system was checked by analyzing the dependence of the pressure on namely and by the behavior of the energy after the equilibration.

The structural properties of the fluid were obtained by inspection of the behavior of the translation order parameter [13–15], defined as

$$t \equiv \int_0^{\xi_c} |g(\xi) - 1| d\xi, \quad \text{where} \quad \begin{cases} \xi = r\rho^{1/3}, \\ \xi_c = r_c\rho^{1/3}, \end{cases} \quad (2)$$

where  $r\rho^{1/3}$  represents the average number of particles at a given distance  $r$  and  $g(\xi)$  is the

radial distribution function. The radial distribution function is given by

$$g(r) = \frac{V}{N^2} \left\langle \sum_{i=1}^N \sum_{j=1, j \neq i}^N \delta(\mathbf{r} - \mathbf{r}_{ij}) \right\rangle, \quad r_{ij} = |\mathbf{r}_i(\tau) - \mathbf{r}_j(\tau)|. \quad (3)$$

where  $\mathbf{r}_i$  and  $\mathbf{r}_j$  are the coordinates of particles  $i$  and  $j$  at time  $\tau$ ,  $V$  and  $N$  are the volume and number of particles respectively and  $\langle \dots \rangle$  denotes an average over all particles.

The dynamical behavior was obtained through the diffusion coefficient  $D$ , related to the mean square displacement (MSD) from Einstein's relation,

$$D^* = \lim_{\tau \rightarrow \infty} \frac{\langle \Delta r(\tau)^2 \rangle}{6\tau}, \quad \langle \Delta r(\tau)^2 \rangle = \langle [\mathbf{r}_i(\tau_0 + \tau) - \mathbf{r}_i(\tau_0)]^2 \rangle, \quad (4)$$

where  $\Delta r$  represent the distance traveled by a particle between two steps of integration of the equation of motion.

The excess entropy, defined as the difference between the entropy of the real fluid and an ideal gas at the same temperature and density was also computed. It can be given by its two body contribution  $s_e$ ,

$$s_e \sim s_2 = -2\pi\rho \int_0^\infty [g(r) \ln g(r) - g(r) + 1] r^2 dr. \quad (5)$$

## B. $\mu VT$ ensemble (GCMC)

In addition to the MD simulations, in order to understand the phase behavior of the gas-liquid transition with the increase of the attractive well Grand Canonical Monte Carlo (GCMC) simulations [59] were employed. The use of the GCMC for this analysis allow us to identify the phase coexistence and the stability of the different phases. In the standard GCMC method the variables chemical potential  $\mu$ , volume  $V$  and temperature  $T$  are fixed, allowing that the total number of particles  $N$  and energy  $U$  fluctuate around of a mean value. Particles can be inserted with probability

$$\mathcal{P}^{\text{acc}}(N \rightarrow N + 1) = \min \left[ 1, \frac{V}{\Lambda^3(N + 1)} e^{\beta(\mu - \Delta U)} \right], \quad (6)$$

removed with probability

$$\mathcal{P}^{\text{acc}}(N \rightarrow N - 1) = \min \left[ 1, \frac{\Lambda^3 N}{V} e^{-\beta(\mu + \Delta U)} \right], \quad (7)$$

and displaced from a initial position  $R_i$  to a final position  $R_f$  with standard Metropolis [60] probability

$$\mathcal{P}^{\text{acc}}(R_i \rightarrow R_f) = \min [1, e^{-\beta\Delta U}] . \quad (8)$$

Here  $\Lambda$  is the de Broglie wavelength,  $\beta = 1/k_B T$  is the inverse of the thermal energy and  $\Delta U$  is the energy difference of the system, resulting from insertion, removing or displacement movement.

In addition to the GCMC simulations the Hyper-Parallel Tempering Monte Carlo (HPTMC) [61] method was performed. The two complementary approaches are relevant to avoid metastable state. The idea is to use the configurations of high temperature to explore the region below the critical temperature, obtaining good statistics for the gas-liquid coexistence. The HPTMC is composed of two steps: in the first step,  $N_r$  replicas of the system, at different thermodynamic states, are simulated in parallel using the standard GCMC procedure. Each different thermodynamic state is characterized by values of  $\{U_i, N_i, \mu_i, T_i\}$  in the range  $\{T_1, \dots, T_{N_r}\}$  and  $\{\mu_1, \dots, \mu_{N_r}\}$ . In the second part, arbitrary pairs of replicas have their configurations exchanged with probability [54, 61]

$$\mathcal{P}^{\text{acc}}(i \longleftrightarrow j) = \min [1, \exp\{(\beta_j \mu_j - \beta_i \mu_i)(N_i - N_j) - (\beta_i - \beta_j)[U_i - U_j]\}] . \quad (9)$$

A variable number of replicas depending on the case studied was adopted. In the GCMC simulations  $5 \times 10^7$  MC steps to equilibration and  $10^8$  MC steps to data production were employed. The simulations were performed for four box sizes:  $L^* = 10, 12, 15$  e  $18$ . For simplicity, only the probability  $P(x)$  for the biggest  $L^*$  size was used.

The critical properties were obtained using the histogram reweighting [62] method. The histogram reweighting is a technique that allow us to obtain thermodynamic averages of a specific state of system from the trajectory of the other state of system. To this end, multiple histograms in number of particles  $N$  and energy  $U$  are combined, for a region with overlap between the histograms [47]. Thus, the probability  $\wp(N, U; \mu, \beta)$  of observe  $N$  particles with energy  $U$  is given by

$$\wp(N, U; \mu, \beta) = \frac{\sum_{i=1}^R f_i(N, U) \exp[-\beta U + \beta \mu N]}{\sum_{i=1}^R K_i \exp[-\beta_i U + \beta_i \mu_i N - C_i]} . \quad (10)$$

In this equation  $K_i$  is the total number of observations for a particular run,  $f_i(N, U)$  is the absolute number of observations of  $N$  particles with energy  $U$  for a particular run, and the constants  $C_i$  are the “weights”, which are obtained by the equation

$$\exp[C_i] = \sum_E \sum_N \wp(N, U; \mu_i, \beta_i) . \quad (11)$$

The absolute pressure was then obtained using the difference between the “weights” of two different thermodynamic states [62]. If the states are characterized by  $(\mu_1, V, \beta_1)$  and  $(\mu_2, V, \beta_2)$ , the pressure is obtained by

$$C_2 - C_1 = \ln \frac{\Xi(\mu_2, V, \beta_2)}{\Xi(\mu_1, V, \beta_1)} = \beta_2 p_2 V - \beta_1 p_1 V . \quad (12)$$

Hence, to estimate the pressure for a specific run, a pressure for reference was used. For instance, at low densities we employed the value given by the ideal gas pressure  $p = \rho k_B T$ .

All physical quantities are shown in reduced units [54] as

$$\begin{aligned} r^* &= \frac{r}{\sigma} \\ U^* &= \frac{U}{\epsilon} \\ \tau^* &= \frac{(\epsilon/m)^{1/2}}{\sigma} \tau \\ T^* &= \frac{k_B T}{\epsilon} \\ p^* &= \frac{\sigma^3}{\epsilon} p \\ \rho^* &= \sigma^3 \rho \\ D^* &= \frac{(m/\epsilon)^{1/2}}{\sigma} D \\ c_V^* &= \frac{c_V}{k_B} . \end{aligned} \quad (13)$$

## IV. RESULTS

First, we explore the effects of the attractive energy of the pair potential in the presence of the density anomaly and in the existence of a liquid-liquid critical.

The figure 3 illustrates the pressure versus temperature phase diagram for the four potentials analyzed. As the attractive part of the potential becomes deeper, the liquid-liquid critical point appears. The appearance of the liquid-liquid phase transition is also related



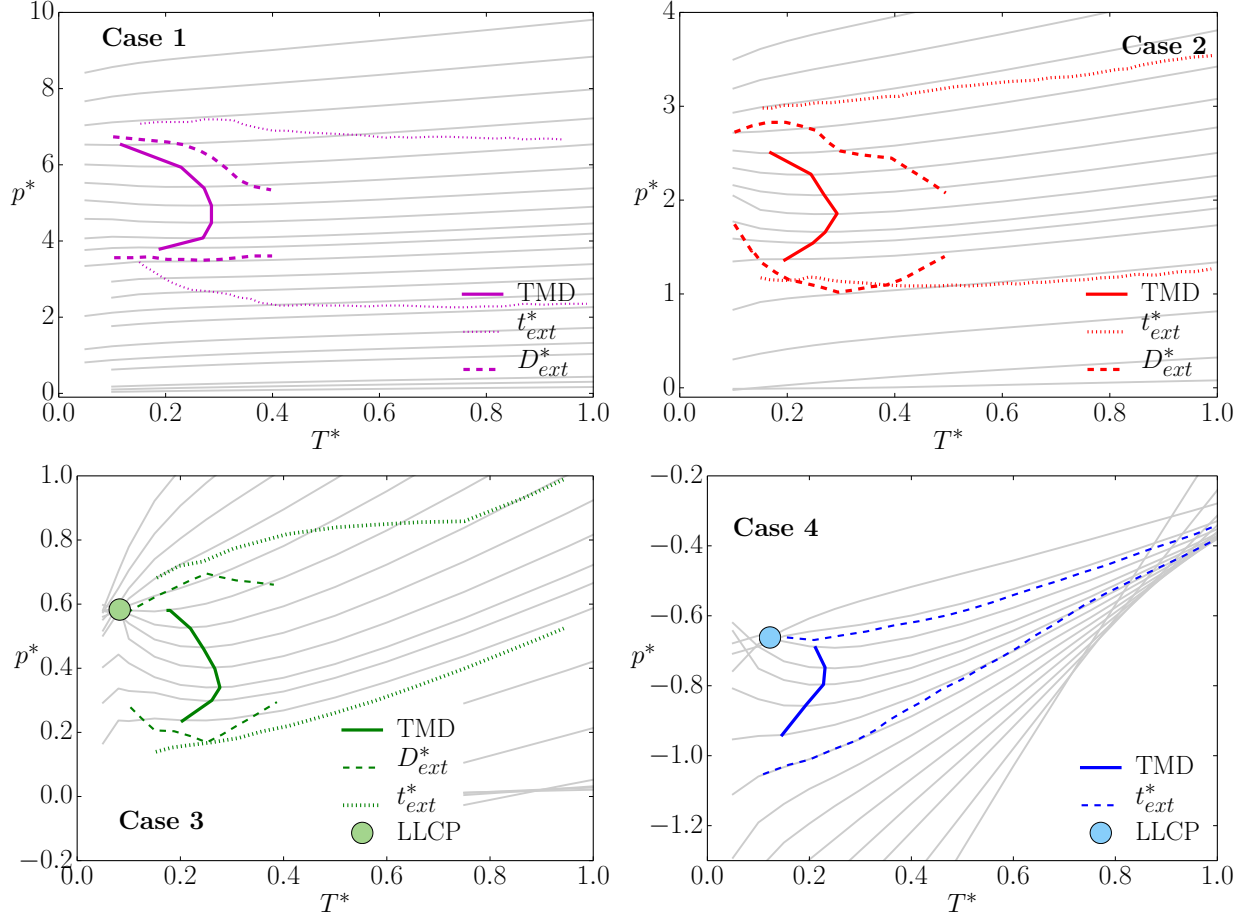


FIG. 3. Pressure versus temperature phase diagram for all the potentials studied. The gray lines are the  $\rho_1^* = 0.0284, \dots, 0.652$ ,  $\rho_2^* = 0.046, \dots, 0.652$ ,  $\rho_3^* = 0.046, \dots, 0.81$  and  $\rho_4^* = 0.30, \dots, 0.81$  are isochores, the solid lines represent the TMD (temperature of maximum density), the dashed lines are the extrema in diffusion coefficient and the dotted lines are extrema in translational order parameter. The circles represent the liquid-liquid critical points for the cases 3 ( $p_C^* = 0.5831$ ,  $T_C^* = 0.0824$ ) and 4 ( $p_C^* = -0.6620$ ,  $T_C^* = 0.1227$ ).

to the shrink in pressure of the TMD line as shown by the figure 4. Our results supports previous results that indicate that the presence of two length scales with one attractive part is necessary but not sufficient for the existence of two liquid phases [52, 53].

The condition, as suggested by Jagla [55], for the presence of the two liquid phases is that the density for fixed temperatures has to show a non monotonic behavior with pressure. Here we explore if this condition also holds for our system in which the two length scales are present but with continuous forces 2.

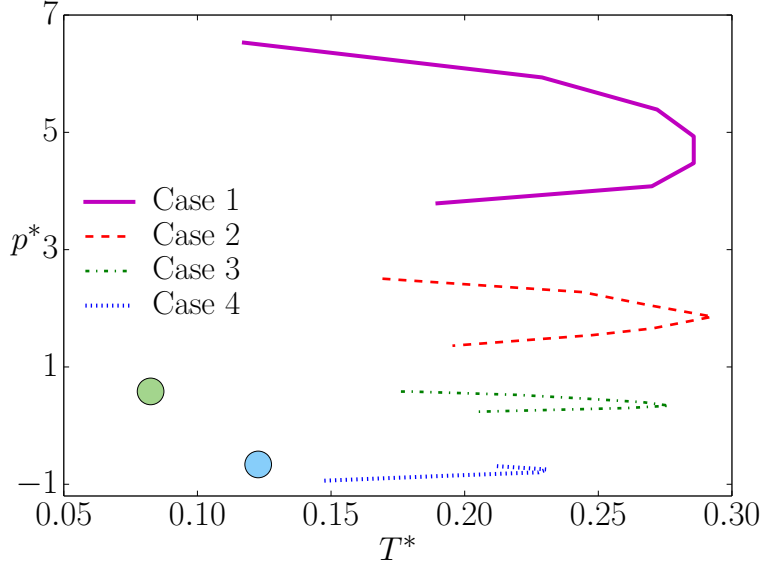


FIG. 4. Pressure versus temperature phase diagram showing the TMD lines for all the potentials studied and critical points for the case 3 (green) and case 4 (blue).

Figure 5 illustrates the pressure versus density isotherms. For clarity the pressures were shifted as  $p^* = n \times p^*$ , where  $n = 1, 2, \dots$  are used for increasing temperatures. In our system, as in the Jagla's potential the increase of the attractive part of the pair potential contributes to negative pressure until a critical value. In this region the density versus pressure at constant temperature becomes reentrant, resulting in a first-order phase transition and a second critical point. In the case 1 where no liquid-liquid critical point is present the density increases with the pressure monotonically while in the case 3 in which the critical point appears in a range of temperatures the pressure becomes reentrant.

Although the anomaly in density is present in all the potentials analyzed, as the potential becomes more attractive, the region in pressure occupied by the TMD decreases. This result is a consequence of the link between the TMD curvature and the presence of phase separation.

Another consequence of the link between criticality and the anomalous behavior is the region in pressure occupied by the dynamic and structural anomalies illustrated as the dashed and dotted lines respectively in the figure 3 shrinks in pressure as the potential becomes more attractive. These thermodynamic, dynamic and structural anomalies are related by the radial distribution function as follows. The radial distribution function  $g(r)$  is a measure of a probability of finding a pair of particles at a given distance  $r$ , which can be evaluated by equation (3), and its behavior is a key ingredient for the presence of the

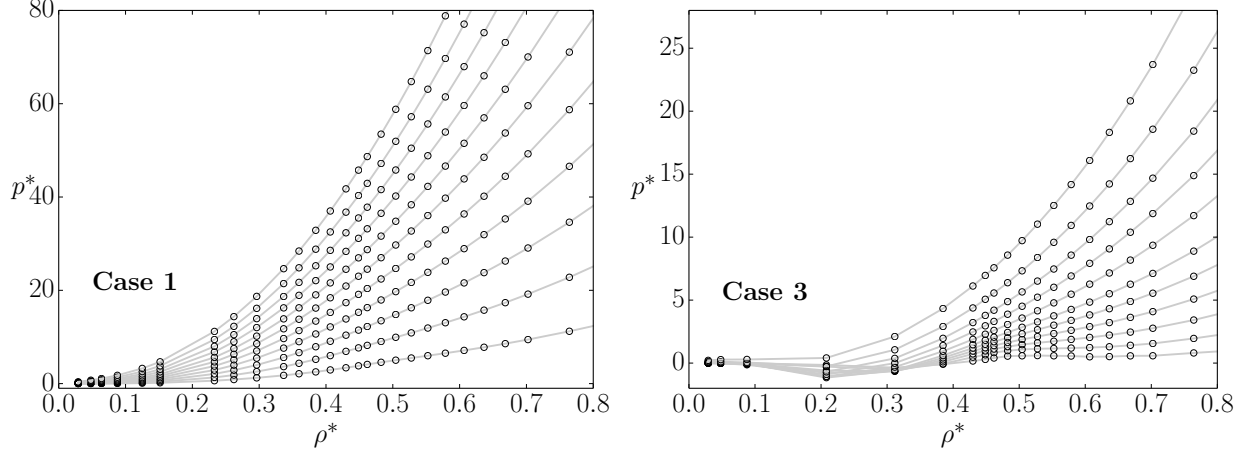


FIG. 5. Pressure versus density phase diagram for the potentials case 1 (left) and the case 3 (right). The circles represent the simulation data and the solid gray lines are guides to the eyes. On the insets, we show the region where the isotherms cross. The range of the temperatures shown on the insets are  $0.1 < T^* < 0.4$  and  $0.15 < T^* < 0.5$  for cases 1 and 3, respectively.

anomalies.

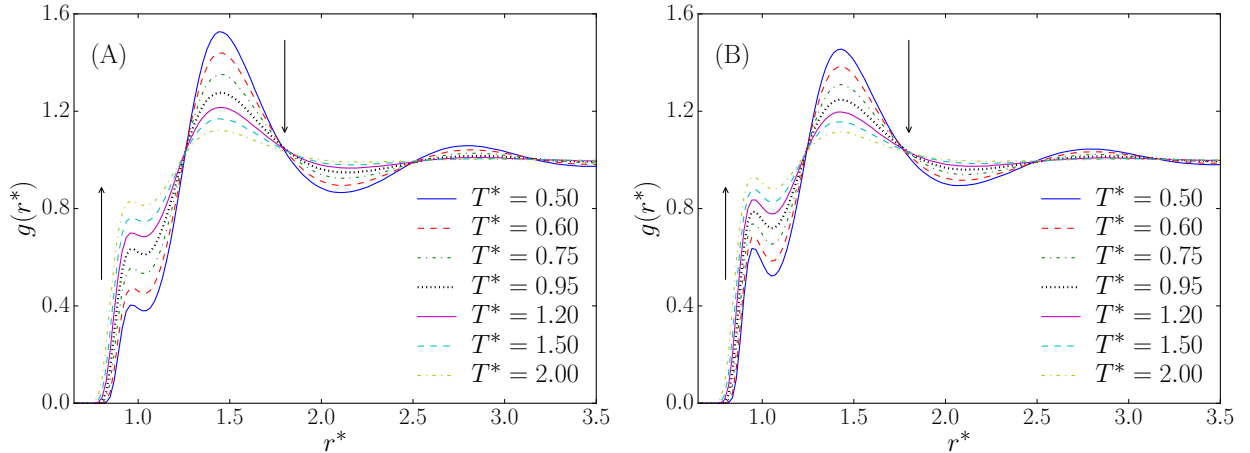


FIG. 6. Radial distribution function as a function of radial distance, for the (A) Case 3 at  $\rho^* = 0.380$  and (B) Case 4 at  $\rho^* = 0.430$ . The arrows indicate the inversion of the highest value of  $g(r^*)$  for each isotherm analyzed.

The figure 6 illustrates the  $g(r)$  as a function of the distance for different temperatures for the potentials case less ideal-gas-like with the increase of the density. As the temperature is increased the mean distance between particles decreases and, as a consequence, the first peak of  $g(r)$  increases while the second peak decreases. Particles changing from the one

length scale to the other is the characteristic of the density anomaly. [26, 50–52].

The unusual behavior of the  $g(r)$  also reflects in the structure. The translational order parameter  $t^*$ , as defined in the equation (2) measures how structured is the system. For the ideal gas, for example, we have  $g(\xi) = 1, \forall \xi$ , and thus  $t = 0$ .

crystallized systems, where the particles have a well defined structure, we have  $g(\xi) \neq 1$  and then  $t \neq 0$ . Therefore, for normal liquids,  $t$  increases with the increasing of density, since an increasing in density induces structuration in system.

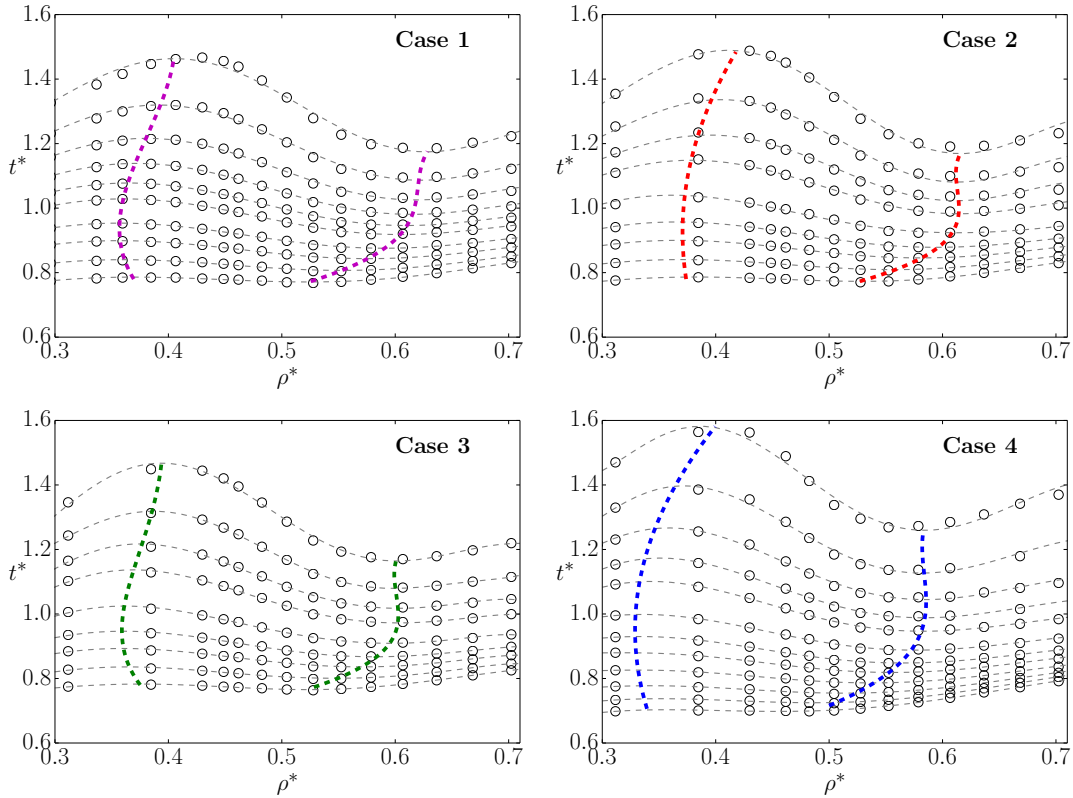


FIG. 7. Translational order parameter versus density for  $T_1^* = 0.100, 0.150, \dots, 0.300, 0.400, \dots, 0.950, 1.20, 1.50$ ,  $T_2^* = 0.15, 0.20, 0.25, \dots, 0.95$ ,  $T_3^* = 0.15, 0.20, 0.25, \dots, 1.50$ ,  $T_4^* = 0.15, 0.20, 0.25, \dots, 0.95$  for the four potentials. The solid gray lines are polynomial fit and circles are points obtained by simulation. Dashed lines denotes the limit of the anomalous region.

The figure 7 shows the translational order parameter as a function of the reduced density for fixed temperatures for all the cases studied. There is a region where in densities in which the parameter  $t^*$  decreases as the density increases, what is the signature of the anomaly.

The increase of the attractive part in the potential hinders the movement between the two scales, reducing the manifestation of the anomaly in  $t$ . Similar results were obtained by Barraz *et al.* [50] for an isotropic water-like model.

The diffusion is computed from equation 4. For normal systems the diffusion decreases with the increase of the density. Figure 8 shows the behavior of the translational diffusion coefficient  $D^*$ , as a function of the reduced density  $\rho^*$ , at constant temperature. For the cases 1, 2 and 3 the systems show a region in which the diffusion increases with the increase of the density what characterizes the diffusion anomaly. As the attractive part of the potential becomes larger, the value of  $D$  in which the anomalous behavior is observed decreases and the region in pressures for the anomalous behavior also shrinks. The mobility of the particles are strongly affected by the depth of the potential.

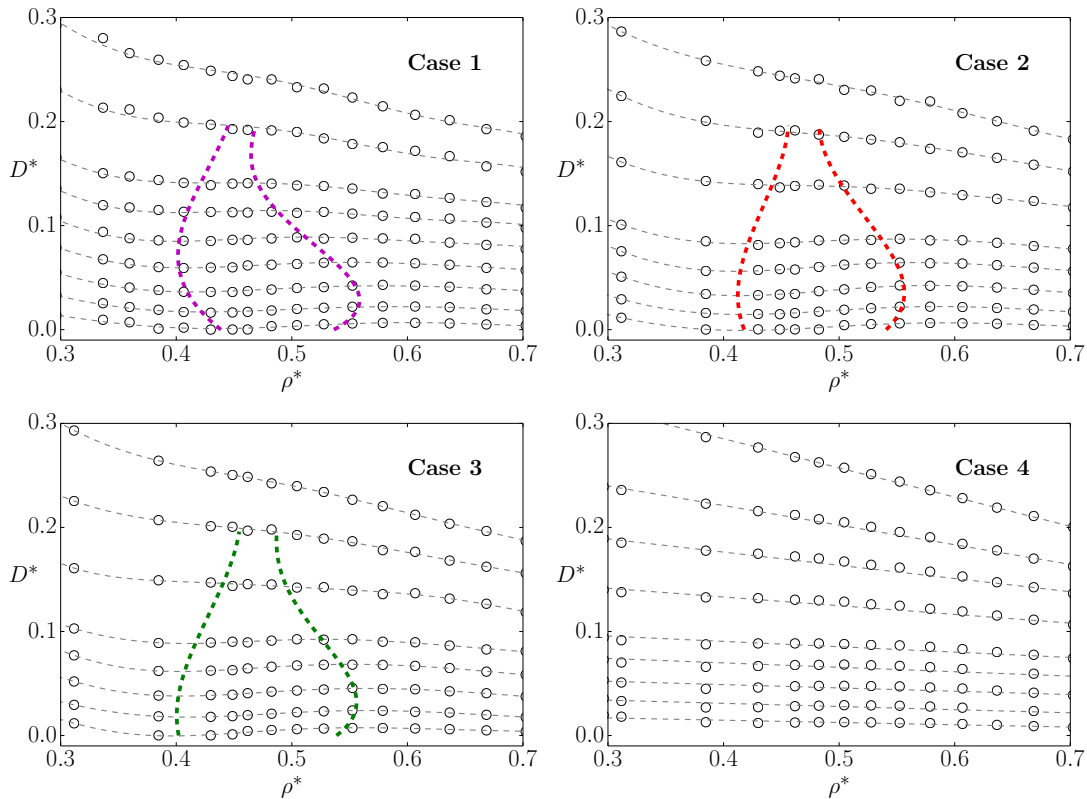


FIG. 8. Diffusion coefficient as function of density for  $T_1^* = 0.20, \dots, 2.50$ ,  $T_2^* = 0.05, \dots, 2.500$ ,  $T_3^* = 0.5, \dots, 2.50$ ,  $T_4^* = 0.05, \dots, 2.50$  and  $T_5^* = 0.1, \dots, 1.05$  for all the potentials studied. The solid gray lines are polynomial fits and circles are points obtained by simulations. Dashed lines denote the region of the anomalous behavior in  $D^*$ .

Here we study a excess entropy defined by equation (5). The excess entropy measures the decreasing of the entropy of the real liquid, when compared to an ideal gas at the same temperature and density, due to structural correlations. If a system has no anomaly, there is no preference of particles to assume a specific coordination shell [63]. However, we observe that for our model the particles move from the second coordination shell to the first coordination one. The structural correlation between the particles can be captured by the excess entropy.

Related to the hierarchy of anomalies the excess entropy is computed from equation 5. For normal liquids the excess of entropy decreases with the increase of the density since the system becomes more structured with the increase of density. Figure 9 shows that for our potentials there is a region in densities in which the excess entropy increases with the increase of density what characterizes the region of densities in which the system has anomalous behavior. As in the density, diffusion and translational anomalous behavior, this region shrinks in pressure range as the system becomes more attractive.

The use of the NVT molecular dynamic described above is very useful for understanding the anomalous behavior and for locating the critical point. However this method is not manageable for obtaining the coexistence line and the universality class of the transition.

In order to understand the nature of the phases produced by the effective potentials studied in the work, Grand Canonical Monte Carlo analysis was employed. First, the liquid-gas phase transition was analyzed. Using the estimates of the critical region and critical histograms obtained from simulations, the low and the high density histograms were combined to obtain the coexistence region, as shown in figure 10.

The density versus temperature phase diagram, figure 10, shows an increase of the critical temperature and density when the attractive scale becomes deeper. Then using the method described in the section III the pressure of the liquid-gas critical point was obtained. The figure 11 illustrates the pressure versus temperature phase diagram of the liquid-gas coexistence and it shows that as the attractive part of the potential becomes deeper, the temperature and the pressure of the liquid-gas critical point increases what is natural since more temperature is required to form the fluid phase. A similar result was found for a spherical potential with two length scales by MD simulations [52].

The nature of the liquid-gas phase transition is Ising-like since the method we have used to characterize the gas-liquid critical point is based on an Ising 3D universality class

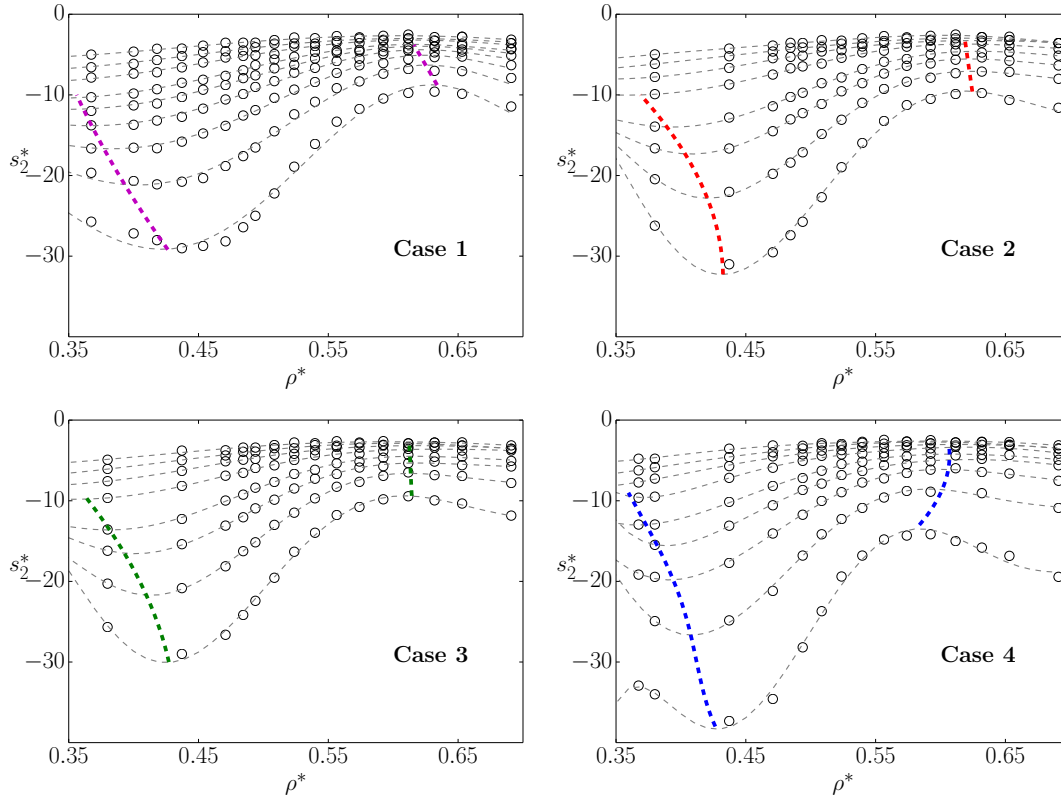


FIG. 9. Excess entropy versus density for  $T_1^* = 0.20, \dots, 2.50$ ,  $T_2^* = 0.05, \dots, 2.500$ ,  $T_3^* = 0.5, \dots, 2.50$ ,  $T_4^* = 0.05, \dots, 2.50$  and  $T_5^* = 0.1, \dots, 1.05$ . The gray solid lines are polynomial fit and circles are simulational points. Dashed lines comprise the anomalous region.

hypothesis. The figure. 12 illustrates the normalized probability distribution,  $P(x)$ , which has an universal form at criticality represented by  $x = A(M - M_c)$  where  $A$  is the non-universal constant and the critical value of the ordering operator  $M_c$  were chosen so that the data have zero mean and unit variance. For one-components systems the ordering operator,  $M$ , is proportional to a linear combination of the number of particles  $N$  and the system total configurational energy  $U$ , given by

$$M \propto N - sU, \quad (14)$$

where  $s$  is the field-mixing parameter [64]. This approach is appropriated only if the symmetry of the order parameter is Ising-like.

The figure 10 also shows for high densities a plateau that suggests the presence of a coexistence between two high density phases. Unfortunately these transition does no appear clearly in the method we are employing, possible for not being Ising-like. In order to obtain

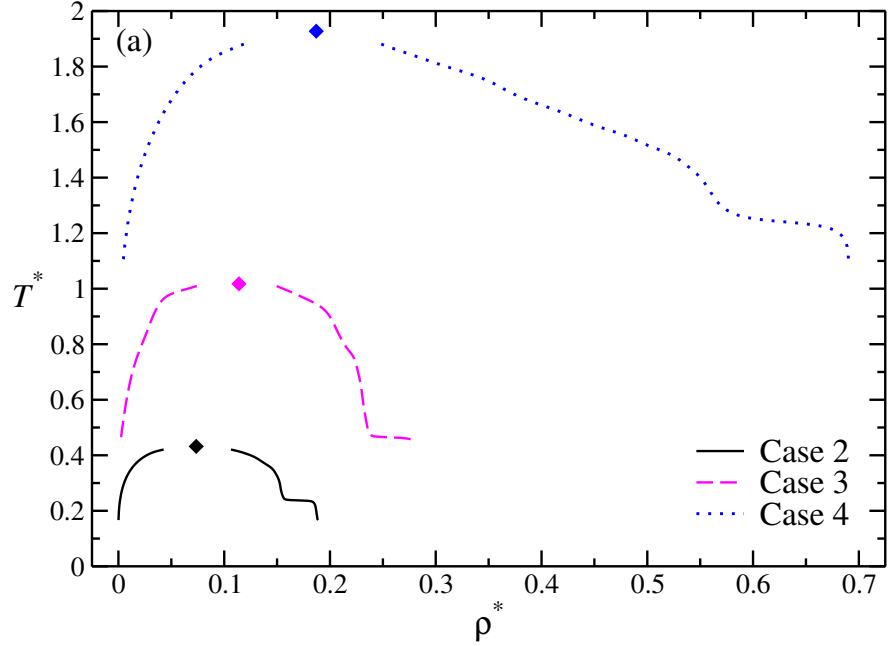


FIG. 10. Density versus temperature phase diagram for the liquid gas coexistence for the three potentials with an attractive part.

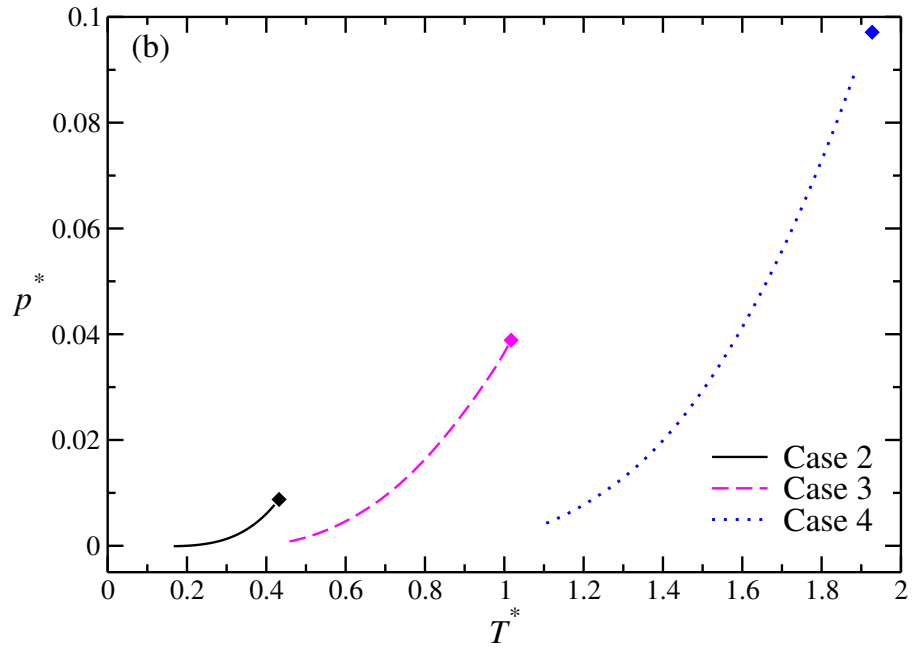


FIG. 11. Pressure versus temperature phase diagram for the liquid gas coexistence for the three potentials with an attractive part.

some evidence of the existence of another type of transition in addition to the liquid-gas, the behavior density versus chemical potential was computed using Grand Canonical Monte



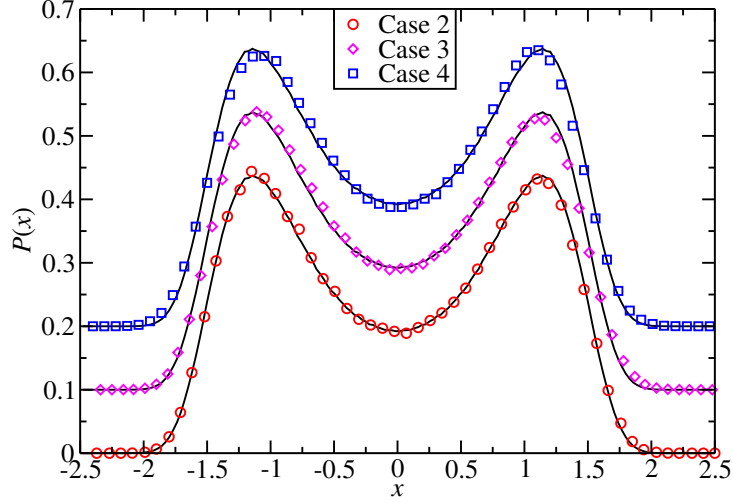


FIG. 12. Comparison between the probability  $P(x)$  for the the case 2 (circles), 3 (diamond) and 4 (squares). The full line represents the universal curve for the Ising 3D universality class for  $L^* = 18$ .

Carlo without the use of the Ising 3D universality class hypothesis.

The figure 13 illustrates the density versus chemical potential for a fixed temperature showing a discontinuous change in density from the gas to the liquid and then between two liquids of high density. The transition is first order.

A more clear picture of the nature of the transition is obtained by computing the specific heat at constant volume. In the grand canonical simulations  $c_V$  is obtained by using the expression [54]

$$c_V = \frac{3}{2}k_B + \frac{1}{Nk_B T^2} \left( \langle \Delta U^2 \rangle_{\mu VT} - \frac{\langle \Delta U \Delta N \rangle_{\mu VT}^2}{\langle \Delta N^2 \rangle_{\mu VT}} \right). \quad (15)$$

The figure 14 shows the behavior of the specific heat versus chemical potential at constant temperature for the three cases in which the potential shows an attractive part. The graphs show a large peak in the specific heat that coincides with the liquid-gas phase transition and a small peak that coincides with the plateau in the figure 10. As the temperature is increased the large peak gives rise to the liquid-gas critical point but the small peak vanishes. This result suggests that the phase observed in this region is either solid or amorphous. Unfortunately lower temperature analysis is not feasible due to the slowing down. In the Monte Carlo analysis no indication of the liquid-liquid phase transition is observed. This might be due to the present of stable solid phases and to the universality

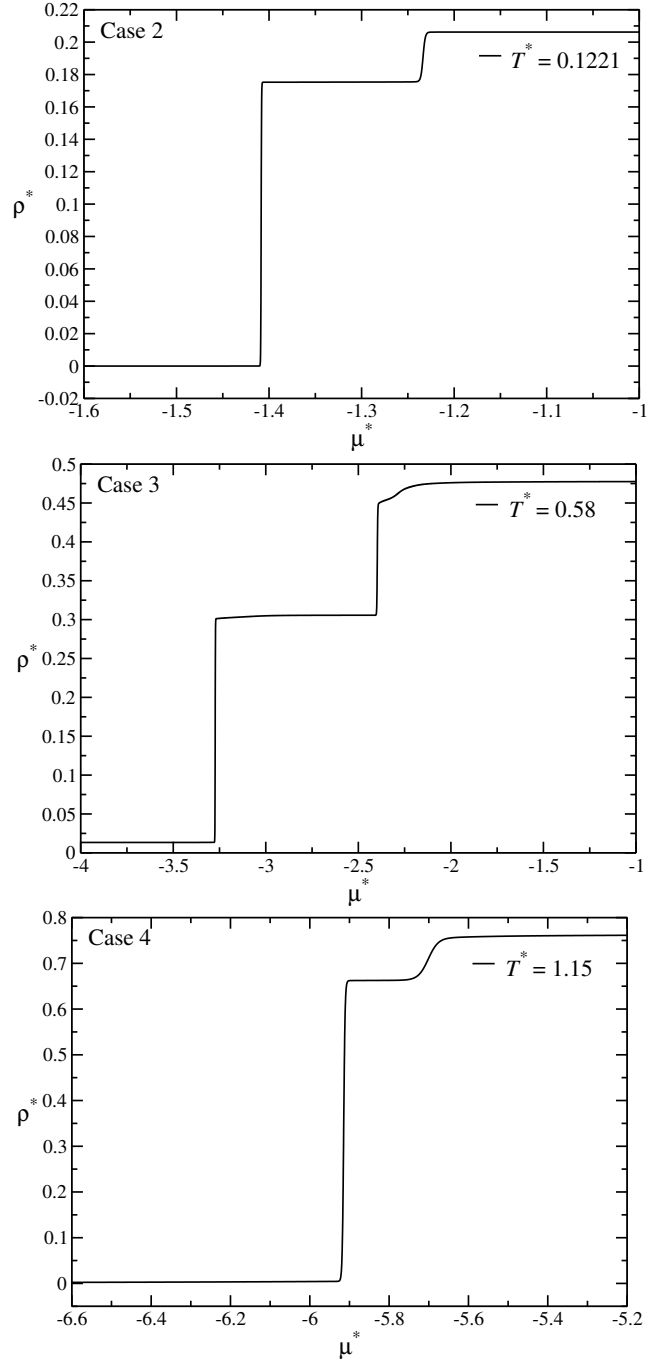


FIG. 13. Density versus chemical potential for the case 2 at  $T^* = 0.1221$ , case 3 at  $T^* = 0.58$  and case 4 at  $T^* = 1.15$ .

class of the liquid-liquid transition that might not be 3D Ising-like as implied in our method.

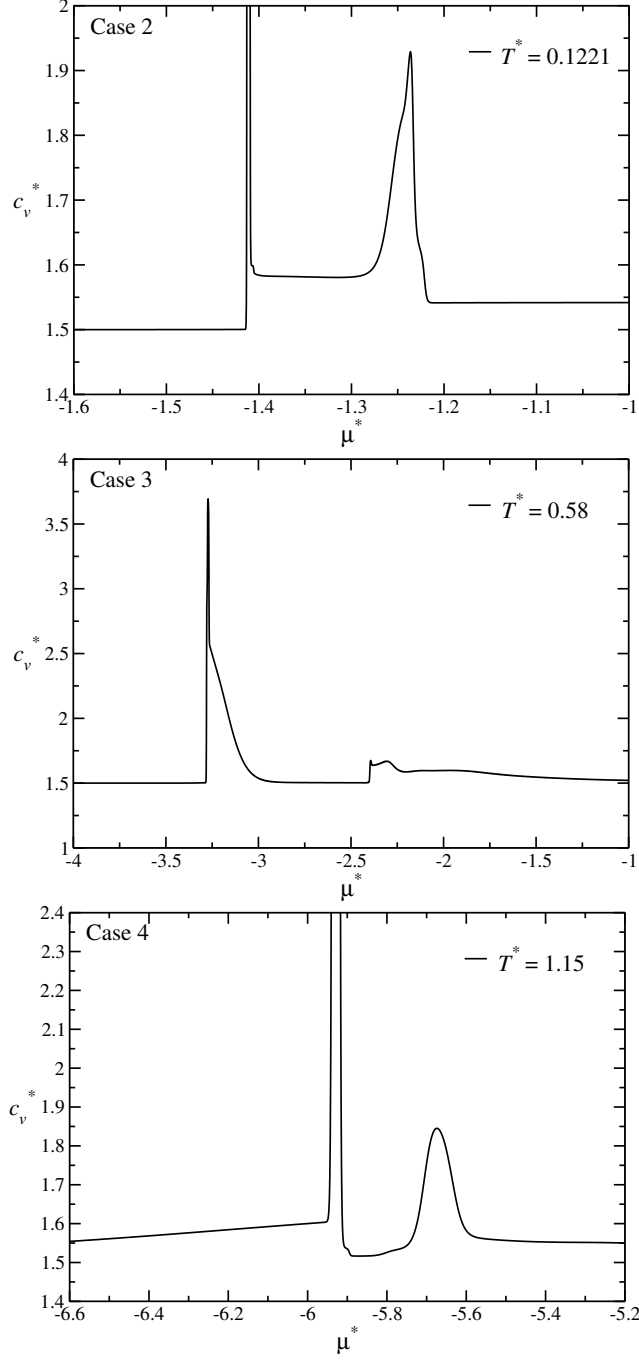


FIG. 14. Specific heat versus chemical potential for the case 2 at  $T^* = 0.1221$ , case 3 at  $T^* = 0.58$  and case 4 at  $T^* = 1.15$ .

## V. CONCLUSIONS

In this paper we analyzed the effect of the attractive part in the pressure versus temperature phase diagram of a family of smooth a core-softened potential with two length scales.

The four potentials analyzed show a repulsive shoulder followed by well that in three cases are attractive. We found that the increase of the attractive scale adds a negative pressure which shrinks the TMD region and it moves it to lower pressures. Related to the shrink of the TMD pressure region, the increase of the attractive well makes the density versus pressure at constant temperature non monotonic and reentrant what is the necessary condition for the appearance of the two liquid phases.

Since all the anomalies are interconnected the attraction also shrinks the pressure range of the structural order parameter, diffusion anomaly and excess entropy.

In order to understand the nature of the liquid-gas phase transition of the core-softened potentials, the three systems in which attraction is present were analyzed using GCMC. We show that the liquid-gas phase transition is Ising like and the critical temperature increases with the increase of the attractive well in the potential. The Monte Carlo analysis does not show the presence of the liquid-liquid phase transition what can be attributed to two effects: the method employed that assume that the transition is 3D Ising and the presence of solid or amorphous phases are present obscuring the high density liquid phase that might be metastable.

## ACKNOWLEDGMENTS

We tank for financial support the Brazilian science agencies CNPq, CAPES and INCT-FCx and Centro de Física Computacional IF(CFCIF) for computational support.

- 
- [1] E. Lomba, N. G. Almarza, C. Martin, and C. McBride, *J. Chem. Phys.* **126**, 244510 (2007).
  - [2] R. Waler, *Essays of natural experiments* (Johnson Reprint, New York, 1964).
  - [3] G. S. Kell, *J. Chem. Eng. Data* **20**, 97 (1975).
  - [4] C. A. Angell, E. D. Finch, and P. Bach, *J. Chem. Phys.* **65**, 3063 (1976).
  - [5] F. X. Prielmeier, E. W. Lang, R. J. Speedy, and H. D. Ludemann, *Phys. Rev. Lett.* **59**, 1128 (1987).
  - [6] H. J. C. Berendsen, J. R. Grigera, and T. P. Straatsma, *J. Phys. Chem.* **91**, 6269 (1987).
  - [7] P. H. Poole, F. Sciortino, U. Essmann, and H. E. Stanley, *Nature (London)* **360**, 324 (1992).

- [8] G. Franzese, A. Hernando-Martínez, P. Kumar, M. G. Mazza, K. Stokely, E. G. Strekalova, F. de los Santos, and H. E. Stanley, *Journal of Physics: Condensed Matter* **22**, 284103 (2010).
- [9] G. Franzese and H. E. Stanley, *J. Phys.: Cond. Matter* **14**, 2201 (2002).
- [10] G. Franzese and H. E. Stanley, *J. Phys.: Cond. Matter* **19**, 205126 (2007).
- [11] G. Franzese, M. I. Marques, and H. E. Stanley, *Phys. Rev. E* **67**, 011103 (2003).
- [12] P. Kumar, G. Franzese, and H. E. Stanley, *Phys. Rev. Lett.* **100**, 105701 (2008).
- [13] M. S. Shell, P. G. Debenedetti, and A. Z. Panagiotopoulos, *Phys. Rev. E* **66**, 011202 (2002).
- [14] J. R. Errington and P. G. Debenedetti, *Nature* **409**, 4 (2001).
- [15] J. R. Errington, *The Journal of Chemical Physics* **118**, 9915 (2003).
- [16] R. Sharma, S. N. Chakraborty, and C. Chakravarty, *J. Chem. Phys.* **125**, 204501 (2006).
- [17] M. Agarwal, M. Singh, R. Sharma, M. Parvez Alam, and C. Chakravarty, *The Journal of Physical Chemistry B* **114**, 6995 (2010).
- [18] M. Agarwal, M. P. Alam, and C. Chakravarty, *The Journal of Physical Chemistry B* **115**, 6935 (2011).
- [19] A. B. de Oliveira, P. A. Netz, T. Colla, and M. C. Barbosa, *J. Chem. Phys.* **124**, 084505 (2006).
- [20] A. B. de Oliveira, P. A. Netz, T. Colla, and M. C. Barbosa, *J. Chem. Phys.* **125**, 124503 (2006).
- [21] A. B. de Oliveira, M. C. Barbosa, and P. A. Netz, *Physica A* **386**, 744 (2007).
- [22] A. B. de Oliveira, E. B. Neves, C. Gavazzoni, J. Z. Paukowski, P. A. Netz, and M. C. Barbosa, *J. Chem. Phys.* **132**, 164505 (2010).
- [23] J. R. Errington, T. M. Truskett, and J. Mittal, *J. Chem. Phys.* **125**, 244502 (2006).
- [24] J. Mittal, J. R. Errington, and T. M. Truskett, *J. Phys. Chem. B* **110**, 18147 (2006).
- [25] Z. Yan, S. V. Buldyrev, P. Kumar, N. Giovambattista, P. G. Debenedetti, and H. E. Stanley, *Phys. Rev. E* **76**, 051201 (2007).
- [26] N. Barraz Jr., E. Salcedo, and M. Barbosa, *J. Chem. Phys.* **135**, 104507 (2011).
- [27] H. Thurn and J. Ruska, *J. Non-Cryst. Solids* **22**, 331 (1976).
- [28] *Handbook of Chemistry and Physics*, 65th ed. (CRC Press, Boca Raton, Florida, 1984).
- [29] G. E. Sauer and L. B. Borst, *Science* **158**, 1567 (1967).
- [30] S. J. Kennedy and J. C. Wheeler, *J. Chem. Phys.* **78**, 1523 (1983).
- [31] T. Tsuchiya, *J. Phys. Soc. Jpn.* **60**, 227 (1991).

- [32] C. A. Angell, R. D. Bressel, M. Hemmatti, E. J. Sare, and J. C. Tucker, *Phys. Chem. Chem. Phys.* **2**, 1559 (2000).
- [33] M. Agarwal, R. Sharma, and C. Chakravarty, *The Journal of chemical physics* **127**, 164502 (2007).
- [34] M. Agarwal and C. Chakravarty, *The Journal of Physical Chemistry B* **111**, 13294 (2007).
- [35] P. H. Poole, M. Hemmati, and C. A. Angell, *Phys. Rev. Lett.* **79**, 2281 (1997).
- [36] H. Tanaka, *Phys. Rev. B* **66**, 064202 (2002).
- [37] P. C. Hemmer and G. Stell, *Phys. Rev. Lett.* **24**, 1284 (1970).
- [38] G. Stell and P. C. Hemmer, *J. Chem. Phys.* **56**, 4274 (1972).
- [39] E. A. Jagla, *Phys. Rev. E* **58**, 1478 (1998).
- [40] E. A. Jagla, *J. Chem. Phys.* **110**, 451 (1999).
- [41] E. A. Jagla, *J. Chem. Phys.* **111**, 8980 (1999).
- [42] E. A. Jagla, *Phys. Rev. E* **63**, 061501 (2001).
- [43] P. Kumar, S. V. Buldyrev, F. W. Starr, N. Giovambattista, and H. E. Stanley, *Phys. Rev. E* **72**, 51503 (2005).
- [44] P. Camp, *Phys. Rev. E* **68**, 061506 (2003).
- [45] P. Camp, *Phys. Rev. E* **71**, 031507 (2005).
- [46] N. B. Wilding and J. E. Magee, *Phys. Rev. E* **66**, 031509 (2002).
- [47] H. M. Gibson and N. B. Wilding, *Phys. Rev. E* **73**, 061507 (2006).
- [48] A. B. de Oliveira, P. A. Netz, and M. C. Barbosa, *Euro. Phys. J. B* **64**, 48 (2008).
- [49] A. B. de Oliveira, G. Franzese, P. A. Netz, and M. C. Barbosa, *J. Chem. Phys.* **128**, 064901 (2008).
- [50] N. Barraz Jr., E. Salcedo, and M. Barbosa, *J. Chem. Phys.* **131**, 094504 (2009).
- [51] A. B. de Oliveira, P. A. Netz, and M. C. Barbosa, *Europhys. Lett.* **85**, 36001 (2009).
- [52] J. da Silva, E. Salcedo, A. B. Oliveira, and M. C. Barbosa, *J. Phys. Chem.* **133**, 244506 (2010).
- [53] D. Y. Fomin, N. V. Gribova, V. N. Ryzhov, S. M. Stishov, and D. Frenkel, *J. Chem. Phys.* **129**, 064512 (2008).
- [54] M. P. Allen and D. J. Tildesley, *Computer Simulation of Liquids* (Clarendon Press, New York, NY, USA, 1989).
- [55] E. A. Jagla, *Brazilian Journal of Physics* **34**, 17 (2004).

- [56] L. Xu, S. V. Buldyrev, C. A. Angell, and H. E. Stanley, *Phys. Rev. E* **74**, 031108 (2006).
- [57] W. G. Hoover, *Phys. Rev. A* **31**, 1695 (1985).
- [58] W. G. Hoover, *Phys. Rev. A* **34**, 2499 (1986).
- [59] G. E. Norman and V. S. Filinov, *High Temp.* **7**, 216 (1969).
- [60] N. Metropolis, A. W. Rosenbluth, M. N. Rosenbluth, and A. H. Teller, *J. Chem. Phys.* **21**, 1087 (1953).
- [61] Q. Yan and J. J. de Pablo, *J. Chem. Phys.* **111**, 9509 (1999).
- [62] A. M. Ferrenberg and R. H. Swendsen, *Phys. Rev. Lett.* **61**, 2635 (1988).
- [63] A. B. de Oliveira, E. Salcedo, C. Chakravarty, and M. C. Barbosa, *J. Chem. Phys.* **132**, 234509 (2010).
- [64] A. D. Bruce and N. B. Wilding, *Phys. Rev. Lett.* **68**, 193 (1992).